Desalination 619 (2026) 119544

Contents lists available at ScienceDirect

Desalination

journal homepage: www.elsevier.com/locate/desal

Investigating the influence of polymaleic acid on reverse osmosis membrane performance to mitigate gypsum scaling

Raynara Maria Silva Jacovone [a], Meng Wang [a], Jaqueline Jamara Souza Soares [b], Solange Kazumi Sakata [c,*,1], Debora Frigi Rodrigues [a,b,**,1]

[a] Department of Civil and Environmental Engineering, University of Houston, Houston, TX-77004, USA
[b] Department of Environmental Engineering and Earth Sciences, Clemson University, Clemson, SC, 29634, United States
[c] Nuclear and Energy Research Institute, National Commission of Nuclear Energy (IPEN/CNEN - SP), Sao Paulo, SP 05508-000, Brazil

HIGHLIGHTS

- PMA in solution exhibits higher scaling resistance but lower cleaning efficiency.
- PMA coating improves scaling resistance and maintains better cleaning efficiency.
- XPS confirms distinct Ca-binding modes affecting cleaning and re-scaling performance.
- Rescaling confirms consistent flux decline trends and surface coverage patterns.
- PMA-coated membranes retain greater stability than unmodified ones after cleaning.

GRAPHICAL ABSTRACT

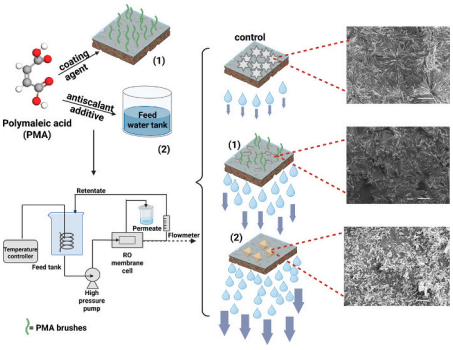

ARTICLE INFO

Keywords:
Reverse osmosis
Polymaleic acid
Gypsum scaling
Membrane cleaning
Anti-scaling

ABSTRACT

Polymaleic acid (PMA) is widely recognized and utilized as an anti-scaling agent in reverse osmosis (RO) applications, however, the specific impacts of PMA on RO membrane scaling and cleaning performance remain underexplored, particularly related to comparing the addition of PMA to the feed solution and its immobilization on membrane surfaces. To address this knowledge gap, this study compared bare membranes alone with membranes coated (ESPA2-PMA) and bare membrane exposed to PMA in the feed solution (ESPA2-PMA_Solution), with all membranes tested under dynamic RO scaling, cleaning, and re-scaling conditions. Initial scaling experiments showed that both PMA applications presented reduced flux declines relative to the unmodified membrane. PMA in solution demonstrated the highest scaling resistance, maintaining up to 70 % of the initial flux after 6 h, while the coated membrane showed moderate improvement. X-ray photoelectron spectroscopy (XPS) analysis revealed that PMA's form—coating versus solution—significantly influenced calcium (Ca) binding modes and gypsum crystal formation process. After cleaning, the membranes treated with PMA in solution had the lowest water recovery, suggesting strong scaling prevention but reduced cleaning efficiency, likely due to Ca bridges forming between gypsum crystals and the membrane surface, which impacted the cleaning process.

* Corresponding author.
** Corresponding author at: Department of Environmental Engineering and Earth Sciences, Clemson University, Clemson, SC, 29634, United States.
E-mail addresses: sksakata@ipen.br (S.K. Sakata), dfrodri@clemson.edu (D.F. Rodrigues).
[1] Equal contribution.

https://doi.org/10.1016/j.desal.2025.119544
Received 29 August 2025; Received in revised form 13 October 2025; Accepted 19 October 2025
Available online 20 October 2025

Rescaling experiments confirmed consistent trends in fouling resistance and cleaning durability. These findings underscore PMA's potential both as a membrane coating and as a feed additive, presenting an effective strategy to minimize gypsum fouling and enhance RO membrane longevity in desalination systems.

1. Introduction

Reverse osmosis is the most energy-efficient technology and the most used worldwide in seawater or brackish water desalination [1,2]. Despite the outstanding performance of RO membranes, their overall capacity for water production is affected by mineral scaling formation, which reduces water flux and salt rejection [3,4]. During the desalination process, diverse inorganic species, such as Ba^{2+}, Ca^{2+}, SO_4^{2-} and HCO_3^-, present in the feed water, may surpass their solubility limits, resulting in the formation of mineral scaling, including $BaSO_4$, $CaSO_4$, and $CaCO_3$ [5,6]. Among those inorganic scales, calcium sulfate ($CaSO_4$), also known as gypsum, is hard to remove in RO systems because its solubility doesn't change much with pH [3,7].

Currently, the addition of antiscalants into the feed water tank in the RO system is the most common and effective approach to minimize gypsum scaling. Anionic polymers, such as polyacrylic acid (PAA) and polymaleic acid, have been extensively employed as antiscalants to prevent gypsum formation [8–10]. The effectiveness of these two polymers as gypsum scaling inhibitors is due to the carboxylic groups (-COOH) present in their side chains, which interact with the calcium ions, distorting the crystal structure or delaying further growth and agglomeration of gypsum crystals. For instance, Amjad and Koutsoukos [9] reported PMA's ability to inhibit the precipitation of gypsum from supersaturated solutions with polymer concentrations as low as 2 ppm.

Besides dosing antiscalants in the feed solution, membrane surface modifications have been suggested as a promising alternative strategy to mitigate gypsum scaling in reverse osmosis systems [1,3,11]. Antifouling coatings are seen as a more environmentally friendly and economical alternative to antiscalants, as they reduce the need for chemical additives during desalination, lowering both discharge and operating costs. Numerous studies have demonstrated a strong correlation between membrane surface properties and fouling propensity. Among these properties, hydrophilicity and surface roughness have been identified as the two most critical factors influencing membrane scaling [7,12,13]. Generally, membranes exhibiting higher hydrophilicity and lower surface roughness display superior antifouling characteristics. Therefore, super-hydrophilic materials like polycarboxylates (e.g., PAA) and graphene oxide (GO) have been reported to modify membrane surfaces to mitigate gypsum formation [14]. Compared to GO and PAA, PMA offers several unique advantages: (1) PMA has two carboxylic groups attached to its polymer backbone, which may enhance its gypsum scale inhibition properties compared to PAA; and (2) unlike GO, PMA is easier to apply as a coating, simplifying the membrane modification process and reducing the risk of nanoparticle leaching associated with GO coatings. While the use of PMA as a bulk antiscalant is well documented [9,10,15], few studies have examined its potential as a surface coating. Ashfaq et al. [16] coated a commercial RO membrane with the combination of PMA and GO, and evaluated their resistance to gypsum scaling. However, their study did not include a membrane coated with PMA alone, leaving it unclear whether the improved performance was due to PMA, GO, or their combined effect [16,17]. Moreover, although PMA has been individually studied as a surface modifier or antiscalant, systematic investigations comparing these two modes of application under subsequent scaling have not been reported yet.

To address this gap, we conducted a comprehensive investigation of PMA in both scenarios (coated on the membrane and added in solution) across two consecutive gypsum scaling cycles. Our study also aims to resolve two questions: (1) What are the differences in membrane scaling and cleaning performance between adding PMA to the feed solution and immobilizing it on the membrane surfaces via in situ maleic acid polymerization? (2) How the specific interplay among minerals, PMA, and membrane surface chemistry would control membrane scaling and cleaning efficacy. Our approach uniquely integrates dynamic filtration with sequential scanning electronic microscope (SEM) and X-ray spectroscopy (XPS) characterization after each critical step: first scaling, cleaning, and second scaling. This design allows us to evaluate not only PMA's initial antiscaling performance but also its cleaning efficiency and membrane reusability. By comparing the fouling and recovery behavior across three membrane conditions (bare, PMA-coated, and PMA in solution), this study offers new mechanistic insights into the trade-offs between fixed and mobile antiscalant strategies and their practical implications for long-term RO operation.

2. Materials and methods

2.1. Materials

Maleic acid (MA), potassium persulfate ($K_2S_2O_8$), and acetic acid glacial were purchased from Sigma Aldrich, Mo. Polymaleic acid was purchased from Alfa Chemistry. Calcium chloride ($CaCl_2.2H_2O$) and Sodium sulfate (Na_2SO_4) were purchased from VWR. All chemicals used were ACS grade. Polyethylene frame was purchased from McMaster-Carr and the reverse osmosis membranes with polyamide active layer (ESPA2) were provided by Hydranautics Inc. (Oceanside, CA).

2.2. Grafting polymaleic acid onto ESPA2 membrane surface

Before the experiment, the membranes were immersed into a container with a 25 % (*v*/v) isopropanol solution for 30 min, followed by rinsing with deionized water, then stored at 4 °C until further use. To functionalize the membrane surface, the ESPA2 membranes were clamped between a polyethylene frame and an aluminum sheet to isolate the polyamide active layer of the membrane. Redox radical initiation reaction was used to graft polymaleic acid onto the RO membrane.

In brief, an aqueous maleic acid solution (0.01–1 M) was prepared, followed by the addition of the $K_2S_2O_8$ (0.001–0.01 M) and $Na_2S_2O_5$ (0.001–0.01 M) to the monomer solution. Then, the solution was immediately poured onto the selective layer of the RO membrane for 1 h at room temperature. After that, the solution was removed, and the membranes were washed three times with deionized water (DIW) to remove unreacted monomers and unattached homopolymers [11,18]. The concentration range of KPS and maleic acid used in the in-situ polymerization was chosen based on previous works reported in the literature [11,19,20]. Moreover, Response Surface Methodology (RSM) was used to optimize the amounts of monomer and initiator to obtain the PMA coating onto ESPA2 surface [21,22]. The optimization aimed to maximize both maximum water permeability and the anti-scaling performance. The concentrations of maleic acid and KPS were optimized using RSM, and the different coated membranes produced were experimentally validated in the lab. The optimal coating condition was achieved using 0.5 M of maleic acid and 0.005 M of potassium persulfate, and therefore, this condition was used for all subsequent experiments, with the resulting membrane referred to as ESPA2-PMA throughout this study. It is worth mentioning that the KPS concentration employed is far below the level at which persulfate has been reported to cause RO membrane damage (~0.15 M) and thus did not induce oxidative degradation of the polyamide active layer during the PMA coating process [23]. More details of PMA coating synthesis are described in the

Supporting Information (**Table S1 and Fig. S1 and S2**).

2.3. Physico-chemical characterization of uncoated and coated membranes

To confirm the incorporation of the polymer on the membranes, the presence of functional groups was evaluated by ATR-FTIR before and after the maleic acid polymerization. The spectra were obtained with a nominal spectral resolution of 4 cm^{-1} in transmittance mode from 4000 to 600 (cm^{-1}) wavenumbers using a HgCdTe detector equipped with a Digilab FTS 7000. XPS analysis was performed using a PHI-5800 spectrometer (Physical Electronics, Chanhassen, MN) equipped with a monochromatic Al Kα X-ray source, to evaluate changes in the O 1 s/N 1 s ratio before and after membrane coating with PMA. The density of carboxyl (–COOH) groups present on both unmodified and modified membranes was quantified through the toluidine blue O (TBO) colorimetric method [24]. More details of the TBO method can be seen in the Supporting Information.

Dynamic light scattering (DLS) was used to measure the Surface Zeta (ζ) potential of the membranes in a Zetasizer Nano, (Malvern Industry Ltda). The membranes were analyzed in the ζ-potential cell between two electrodes. A standard solution (pH 9) of polystyrene latex particles (DTS1235, Malvern Instruments) was used as a tracer. The electrophoretic mobility of the tracer was measured at different distances from the membrane, i.e., 125, 250, 500, 750, and 3000 μm, to calculate the surface ζ-potential of the membrane [14,25]. The surface hydrophilicity of the bare and coated membrane was evaluated by water contact angle (WCA) measurements using a contact angle goniometer (Data-physics OCA 15EC goniometer) [25].

The morphology of the unmodified and modified membranes, before and after scaling tests were analyzed using SEM at various magnifications performed by Nova NanoSEM 230. The accelerating voltage was 10 k*V*. The samples were coated using a gold sputter coater for 60 s (Denton Desk V). Additionally, the topographical characterization of the surface morphology for bare and coated membranes was conducted through atomic force microscopy (AFM) measurements employing an Innova AFM, from Bruker, using tapping mode. The quantification of surface roughness was performed in triplicate on 10 μm × 10 μm sections of the membrane samples, with data acquisition and analysis by the Nano-scope Analysis 1.5 software [26].

2.4. Membrane transport properties

A bench-scale crossflow RO filtration system (active membrane area: 24.2 cm^2) was used to assess membrane water permeability and sodium chloride (NaCl) rejection (**Fig. S3**). Prior to testing, the membranes were compacted with deionized water (DIW) at a transmembrane pressure of 500 psi until a steady-state permeate flux was achieved. For both sets of experiments, the crossflow velocity was maintained at 21.4 cm/s, and the feed solution temperature was regulated at 25 ± 0.5 °C using a recirculating chiller (Polyscience). The pure water permeability (PWP, $L/m^2/h/bar$) was quantified by dividing the permeate water flow rate, Q_p (L/h), by the effective membrane area, A (m^2), and the transmembrane pressure, ΔP (bar), as shown in **Eq.1**. To measure the salt rejection performance, a 50 mM NaCl solution was filtered. The salt rejection (R) was calculated using **Eq.2**, after determining the salt concentrations in the feed (C_f) and permeate (C_p) streams via conductivity measurements using a VWR symphony B40PCID conductivity meter.

$$PWP = Qp/\Delta P.A \tag{1}$$

$$R = \left(\frac{C_f - C_p}{C_f}\right) \times 100\% \tag{2}$$

2.5. Membrane scaling and characterizations

2.5.1. Solution conditions

Calcium sulfate solutions prepared for scaling experiments contained 20 mM Na_2SO_4 and 20 mM $CaCl_2{\cdot}2H_2O$. The saturation indices (*SI*) (**Eq.3**) were calculated with Geochemist's Workbench (GWB, 11.0. 6, Aqueous Solution LLC), at 25 °C, as shown in **Table S2**,

$$\mathrm{SI} = \log_{10}\left(\left\{Ca^{2+}\right\}\cdot\left\{SO_4^{2-}\right\}/K_{sp}\right). \tag{3}$$

where $\{Ca^{2+}\}$, and $\{SO_4^{2-}\}$ represent ion activity and K_{sp} is the gypsum thermodynamic solubility constant.

The bulk solution was under-saturated for gypsum (SI = −0.13 < 0, $\log_{10}$ scale). However, due to concentration polarization, the local conditions near the membrane surface became mildly supersaturated (SI = 0.02 > 0, log10 scale). More details on concentration polarization, and bulk and local SI calculations can be found in our previous publication [4,27]. Mineral scaling occurs on RO membranes through two distinct pathways [3]: (1) direct crystallization on the membrane surface, known as heterogeneous nucleation, and (2) formation of crystals in the bulk solution followed by their deposition onto the membrane, a process called homogeneous precipitation. Under the present conditions, only heterogeneous gypsum scaling can take place due to the slightly saturated level of the solution near the membrane surface (SI = 0.02).

2.5.2. Mineral scaling and re-scaling experiments

Membrane scaling and cleaning experiments were performed using a bench-scale crossflow reverse osmosis (RO) system with two tanks (**Fig. S3**). One tank served as the reservoir for DIW (feed tank 1), which was used for membrane stabilization and backwashing, while the other tank (feed tank 2) contained a well-mixed salt solution for the mineral scaling step. The detailed procedure involved three key steps: DIW stabilization, mineral scaling, and membrane cleaning. DIW stabilization (**Step I**) refers to flushing DIW through the membrane at 500 psi until the permeate volume collected becomes constant. Subsequently, the mineral scaling process (**Step II**) was carried out for 6 h, during which the permeate volume was continuously collected and measured as a function of time. Following the scaling experiments, membrane cleaning (**Step III**) was performed using DIW until a stable permeate flux was achieved, and then the recovered flux was normalized using the stabilized membrane flux before the scaling. **Step III** was skipped for membrane characterization after scaling. It should be mentioned that following the *in-situ* cleaning process, a second cycle membrane scaling test using the same mineral scaling conditions described above was also conducted to assess the robustness of the membrane for scaling resistance.

To evaluate the anti-scaling efficiency of PMA and compare the differences in scaling resistance when PMA was added to the solution versus when it was immobilized on the membrane surface, three sets of membrane scaling experiments were conducted: (1) Control Group (Bare Membrane - ESPA2): In the first set of experiments, gypsum scaling tests were performed on the bare membrane (referred to as ESPA2) as the control group. (2) PMA in Solution (ESPA2-PMA_ Solution): In the second set, the experimental procedure was similar to the control group, with the key difference being the composition of the feed solution. Here, 5 mg/L of PMA was added to the feed water tank (referred to as ESPA2-PMA_Solution) before mixing with $CaCl_2{\cdot}2H_2O$ and Na_2SO_4 to prevent the premature formation of calcium sulfate nuclei [9]. The concentration of 5 mg/L PMA was chosen as it falls within the reported range (2–20 mg/L) commonly used in the literature for antifouling applications, with most studies using concentrations below 10 mg/L [9,28]. This selection ensures that our study aligns with previous findings while focusing on representative and practical concentration. (3) PMA Immobilized on Membrane Surface (ESPA2-PMA): In the third set, PMA was immobilized directly onto the membrane surface (referred to as ESPA2-PMA). The experimental procedure and

feed solution were the same as in the control group. The primary difference between this set and the second set is the PMA availability—whether it was immobilized on the membrane surface or added to the solution.

In all three sets of experiments, the feed solution was pumped into the RO system with a crossflow velocity of 21.4 cm/s, and the transmembrane pressure was maintained at 500 psi [14]. Each experimental run was carried out under consistent crossflow velocity, temperature, and pressure conditions to ensure accurate comparisons of scaling behavior across the different types of membranes. Additionally, a gypsum rescaling experiment was performed for all three groups, using the same feed solution as in the first cycle, and following the procedures mentioned above. The initial fluxes of ESPA2, ESPA2-PMA, and ESPA2-PMA_Solution in both the first scaling and rescaling experiments were statistically comparable (**Fig. S4**), ensuring a valid basis for comparing scaling behavior across the different membranes. This second cycle of scaling experiments aimed to confirm the reproducibility of our initial results, ensuring that the observed enhanced efficiency of the modified membrane was not a singular occurrence. Moreover, the rescaling tests allowed us to evaluate the long-term effectiveness of the membrane modification and to observe potential changes in membrane performance over time and following cleaning processes. Overall, this experiment design provides valuable insights into the scaling resistance, durability, and cleaning resilience of the PMA-modified membranes.

2.5.3. *Membrane characterizations before and after cleaning*

To characterize the precipitates on the membrane surface, two sets of experiments have been done: (1) one set of experiments skipped the membrane cleaning step as we mentioned above. Then the crystal properties (i.e. mineral phase, morphology) on the membrane surface were characterized. First, the crystallinity of the mineral precipitates formed onto the membranes surface after scaling experiments were analyzed by XRD using MiniFlex 600 diffractometer, from Rigaku, with a Cu anode (40 kV and 15 mA). Then, the samples were characterized using SEM to analyze the crystals' morphology. (2) Another set of experiments were done to characterize the remaining precipitates after the membrane cleaning step. The membrane samples were characterized by FTIR and SEM analysis to assess chemical and physical changes, respectively. XPS analysis of three samples before and after the scaling and after the cleaning were conducted to assess the chemical interactions between the mineral scales and PMA. The XPS analysis was done with a PHI-5800 spectrometer (Physics Electronics, Chanhassen, MN) with a monochromatic Al – K X-ray source. A low resolution with a pass energy of 23.5 eV was used for the wide scan, while a higher resolution with a pass energy of 187.8 eV was used to acquire the photoelectron emissions from the precipitated substrates. Spectrum data were processed using the MultiPak V7.0.1 (ULVAC-PHI, Inc.) and OriginPro 2024 (OriginLab, Northampton, MA). The same characterization procedures were also applied to membranes after a second cycle of rescaling experiments to evaluate the influence of PMA—either immobilized on the membrane surface or added to the feed solution—on gypsum crystal re-growth.

3. Results and discussion

3.1. *Surface characteristics of PMA-modified membranes: Hydrophilicity, charge, and functionalization*

The initial step of this study involved confirming the successful coating of the RO ESPA2 membranes with PMA. Fig. 1 presents the ATR-FTIR spectra of the ESPA2, ESPA2-PMA, and maleic acid in the range of 4000–650 cm^{-1}. The unmodified ESPA2 membrane exhibited characteristic absorption bands associated with its polyamide (PA) backbone. The amide I band (C═O stretching vibration) at 1663 cm^{-1} and the amide II band (N—H bending) at 1541 cm^{-1} are indicative of the amide bonds (-CONH-) formed during the interfacial polymerization of meta-

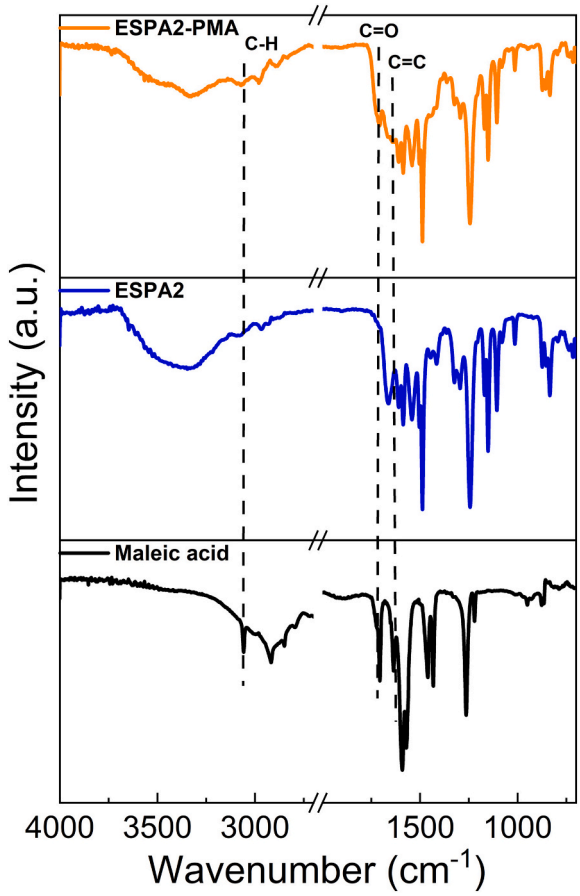

Fig. 1. ATR-FTIR spectra of ESPA2, ESPA2-PMA membranes, and maleic acid.

phenylene diamine (MPD) and trimesoyl chloride (TMC) [29,30]. Additionally, a peak at 1609 cm^{-1}, which can be attributed to C═C stretching vibrations, from the aromatic groups in the polyamide structure. The spectrum of maleic acid exhibited typical bands corresponding to its molecular structure, including the C═O stretching vibration of the carboxyl functional group at 1706 cm^{-1}, as well as stretching modes of C—H and C═C bonds at 3060 cm^{-1} and 1648 cm^{-1}, respectively. After MA polymerization, significant changes were observed in the spectra, confirming the formation of PMA. The C═O stretching of COOH groups present in the monomer structure shifted from 1706 cm^{-1} to 1714 cm^{-1}. This occurred because, during the PMA formation, the C═C bonds present in the MA were converted to C—C in the polymer. Therefore, the C═O was no longer conjugated with a double carbon-carbon bond, which led to a change in the frequency. Additionally, the feature bands at 3060 cm^{-1} and 1648 cm^{-1} disappeared after the polymerization process [17,18]. This result confirmed that the polymer was successfully incorporated on the membrane surface. Notably, no suppression of the N—H stretch (~3330 cm^{-1}) or loss of aromatic C═C vibrations (~1600 cm^{-1}), which are typically associated with oxidative degradation of polyamide membranes by strong oxidants [31], was observed on the ESPA-PMA spectrum, confirming that the KPS-assisted PMA modification did not damage the PA active layer.

To assess the surface hydrophilicity and surface charge of the membranes, WCA and surface zeta potential measurements were conducted on both ESPA2 and ESPA2-PMA membranes, as summarized in Table 1. The bare membrane exhibited a WCA value of 52.1 ± 3.2°, whereas the ESPA2-PMA membrane showed a significantly lower WCA value of 27.4 ± 1.8°. This reduction suggests that PMA coatings enhance the surface hydrophilicity of the bare membrane [4,13,14]. Additionally, the surface charge of the membrane decreased from −37.3 ± 2.7

Table 1
Water contact angle, surface zeta potential, roughness, carboxylic group density, permeability, and salt rejection of unmodified and modified membranes.

Sample	Water contact angle (°)	Surface zeta potential (mV)	Surface roughness (nm)	COOH density (μg/cm^2)	XPS			Permeability (L/m^2.h.bar)	Salt rejection (%)
					C (%)	N (%)	O (%)		
ESPA2	52.1 ± 3.2	- 37.3 ± 2.7	79.4 ± 7.3	0.24 ± 0.97	69.3	11.6	19.1	7.6 ± 1.0	97.8 ± 0.3
ESPA2-PMA	27.4 ± 1.8	- 44.0 ± 2.9	74.4 ± 3.8	0.41 ± 1.65	68.7	9.1	22.2	8.3 ± 0.5	97.7 ± 0.3

mV for the bare membrane to −44.0 ± 2.9 mV after *in-situ* maleic polymerization. These changes in hydrophilicity and surface charge are likely attributed to the introduction of carboxylic functional groups (-COOH) from the PMA coating on the modified membrane [14,27,32]. Comparable trends have been reported in the literature. For example, Ansari et al. [14] modified ESPA2 with PAA and observed that the zeta potential became ~21 % more negative, while the WCA decreased from 32 ± 2° to 28 ± 1°, consistent with the incorporation of carboxyl functionalities. To further confirm this, the surface density of -COOH groups was measured before and after functionalization using the toluidine blue O (TBO) method (**Fig. S5**). As shown in Table 1, after *in-situ* maleic acid polymerization, the density of -COOH groups on the modified membrane nearly doubled (0.412 ± 1.65 μg/cm^2) compared to the unmodified membrane (0.241 ± 0.97 μg/cm^2). Cao et al. [27] likewise observed an increase in –COOH density from 0.14 ± 0.02 μg/cm^2 for ESPA2 to 0.32 ± 0.01 μg/cm^2 after GO modification. These parallels reinforce that PMA grafting effectively introduces additional carboxyl groups, thereby enhancing surface hydrophilicity and charge in agreement with previous modification strategies. Furthermore, the increased O 1 s / N 1 s ratio observed in the XPS survey analysis of the PMA-coated membranes (2.4) compared to the bare membranes (1.6) further supports the presence of a higher concentration of carboxylic acid groups in the polymer structure (Table 1).

The surface topography of the membranes was evaluated using atomic force microscopy before and after PMA functionalization, as shown in Fig. 2. The ESPA2-PMA membrane (Fig. 2b) exhibited a slightly lower root mean square roughness (Rq = 74.4 ± 3.8 nm) compared to the unmodified ESPA2 membrane (Rq = 79.4 ± 7.3 nm) (Fig. 2a). A similar trend was observed by Ashfaq et al. [17], where ESPA2 modified with PMA and GO showed a slight reduction in roughness from 74.7 nm (bare) to 70.6 nm. However, given that our roughness values overlapped within their respective error ranges, it is suggested that the PMA coating did not significantly modify the membrane's morphology [30,33]. Instead, the results indicate that the polymerization process produced a thin, conformal coating that followed the existing membrane topography rather than filling surface valleys or creating a thick additional layer. These observations align with the morphological changes observed in SEM, where the coated membrane (Fig. 2c) appeared slightly smoother but retained the overall structural characteristics of the unmodified ESPA2 membrane (Fig. 2d). Therefore, both AFM and SEM images showed that PMA was successfully grafted onto the membrane surface as a conformal coating, modifying its surface chemistry without drastically altering its topography. The hypothesis of the formation of a conformal PMA coating is consistent with previous reports that used persulfate-initiated in situ polymerization [34,35], where surface-confined polymer growth resulted in a uniform coating without significant changes in surface morphology. For instance, Sun et al. [35] demonstrated that sodium persulfate ($Na_2S_2O_8$)-initiated polymerization of polyaniline (PANI) on GaN microwires led to a conformal coating, preserving the underlying structure while modifying surface morphology. Given that sodium persulfate and potassium persulfate decompose into similar sulfate radicals ($SO_4^{\bullet -}$), it is likely that the KPS-initiated polymerization of PMA on ESPA2 membranes followed a comparable mechanism.

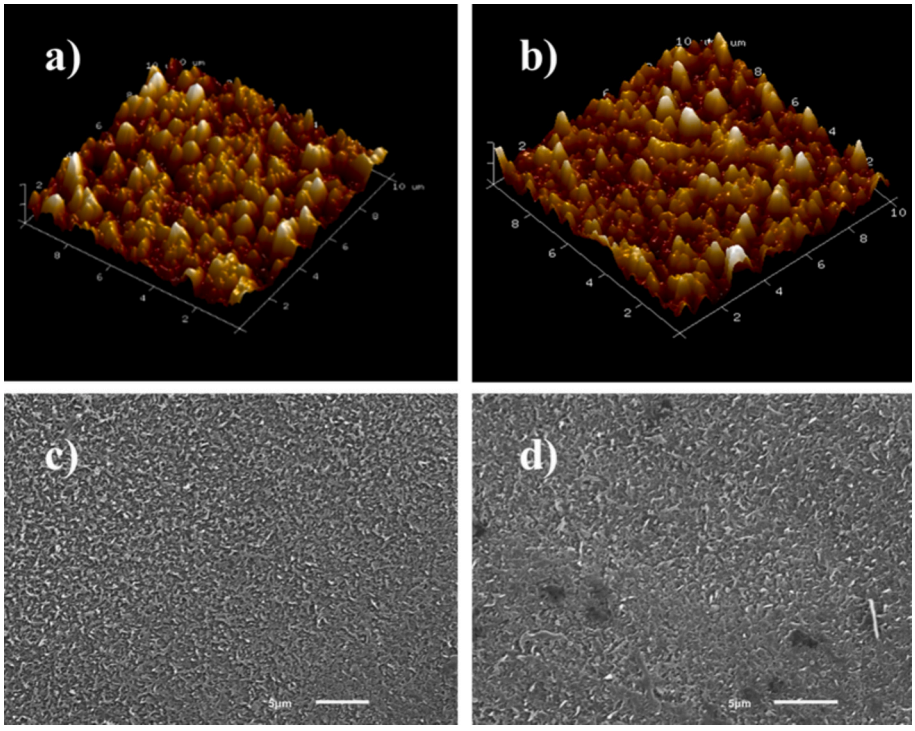

Fig. 2. Microscopic characterization of the membranes. On the upper row, AFM images with scale bar:10 μm, for (a) ESPA2, (b) ESPA2-PMA; on the bottom row, SEM images with scale bar of 5 μm, for (c) ESPA2, (d) ESPA2-PMA.

As shown in Table 1, the water permeability of ESPA2-PMA (8.3 ± 0.5 L m^{-2} h^{-1} bar^{-1}) was slightly higher than that of ESPA2 (7.6 ± 1.0 L m^{-2} h^{-1} bar^{-1}). Although this variation falls within the experimental uncertainty, it indicates that the PMA layer did not introduce significant resistance to mass transfer. At the same time, these values are consistent with the substantial decrease in contact angle and higher carboxyl group density, both of which enhance surface hydrophilicity and facilitate water sorption and diffusion across the membrane. Along with this, the salt rejection of ESPA2-PMA remained nearly identical to that of ESPA2, confirming that the coating did not compromise salt selectivity. Combining with AFM and SEM results showing no major morphological changes, these observations suggest that the PMA layer is thin and uniformly distributed, and that its effect on transport properties is negligible to slightly beneficial. It is worth mentioning that other studies have reported a reduction in membrane permeability following surface modification [17,36]. For example, Ashfaq et al. [17] found that after modifying ESPA2 with PMA and GO, the water permeability decreased, which was attributed to a reduction in pore size caused by polymerization, thereby increasing resistance to permeate flow. In contrast, our results demonstrate that PMA functionalization preserved both permeability and rejection, confirming that the coating did not compromise these critical properties of RO membranes.

3.2. PMA's role in gypsum scaling: Mechanisms and surface interactions

The effect of PMA, both attached to the membrane and in the feed tank solution, in the mineral scaling formation is shown in Fig. 3a. The flux decline rate for unmodified membranes was higher than that of the PMA-modified membranes. Comparison between the non-normalized flux permeate measured at the end of the 6-h scaling experiment showed a decline from 196.65 ± 17.60 (L/ m^2. h) to 20.66 ± 10.52 (L/ m^2. h) for ESPA2 and from 204.07 ± 11.03 (L/ m^2. h) to 56.82 ± 11.39 (L/ m^2. h) for ESPA2-PMA. This observation demonstrated that PMA coatings can mitigate scaling on the membrane surfaces in contrast to bare membranes, due to their improved surface hydrophilicity (Table. 1). According to the classical nucleation theory [37–39], the free energy barrier for heterogeneous nucleation is strongly influenced by the interfacial energy barrier ($\Delta G_{interface}$), which depends on the liquid–substrate interfacial energy (σ_{ls}) as follows (**Eq.4**):

$$\Delta G_{interface} = A_{lp}\sigma_{lp} + A_{sp}\left(\sigma_{sp} - \sigma_{ls}\right) \quad (4)$$

where A_{lp} and A_{sp} are the surface areas of liquid-precipitates and substrate-precipitate interfaces. σ_{lp}, σ_{sp}, and σ_{ls} are the interfacial energies of liquid-precipitate, substrate-precipitate, and liquid- substrate interfaces. It has been reported that σ_{ls} is a key parameter governing heterogeneous precipitation and is closely related to the hydrophilicity of the substrate. A lower σ_{ls} increases the interfacial energy barrier ($\Delta G_{interface}$), making heterogeneous nucleation less favorable on the membrane surface [27,40]. Consequently, compared with the pristine ESPA2 membrane, ESPA2-PMA experienced reduced heterogeneous gypsum precipitation, leading to less surface blockage and a smaller flux decline. This explanation is further supported by our SEM observations, which show more extensive gypsum coverage on ESPA2 than on ESPA2-PMA after the scaling experiments (Fig. 4a-d).

Furthermore, the ESPA2-PMA_Solution membrane exhibited the smallest flux decline among all three experimental conditions. With PMA dosed in the feed solution, the permeate flux after 6 h of scaling remained at approximately 70 % of its initial value, which is significantly higher than that of the control membrane, which dropped to about 15 % over the same period. Yin et al. [11]found that using PAA as an antiscalant in solution was more effective for controlling gypsum scaling in RO desalination than applying PAA as a membrane surface modification. This may be due to differences in polymer behavior in solution versus when coated on surfaces. Free polymer chains generally have greater mobility, meaning that their reactive sites are more available. On the other hand, polymers coated on the surface have restricted movement, and some reactive sites might be less available due to the surface attachment. Another important aspect is related to polymer conformation. Polymers on the surface present more limited conformational changes due to surface interactions and constraints [41,42]. Therefore, calcium ions can diffuse more freely to reactive sites of PMA chains in solution, whereas calcium ion diffusion to PMA-coated membranes can be limited.

To investigate the mineral phase of the precipitates accumulated on the membrane, XRD measurements have been carried out, as shown in **Fig. S6**. It was observed that all samples exhibited the characteristic peaks of gypsum. No other forms of mineral were detected. Therefore, the mineral phase of $CaSO_4$ was not affected by the coatings on the bare membrane. The strongest peak corresponding to the (020) crystal facet was observed on the ESPA2-PMA membrane, while the (021) crystal facet showed the highest intensity on the bare membrane. This suggests that the PMA coating may alter the morphology of gypsum crystals formed on the membrane surfaces [43]. To confirm this hypothesis, the

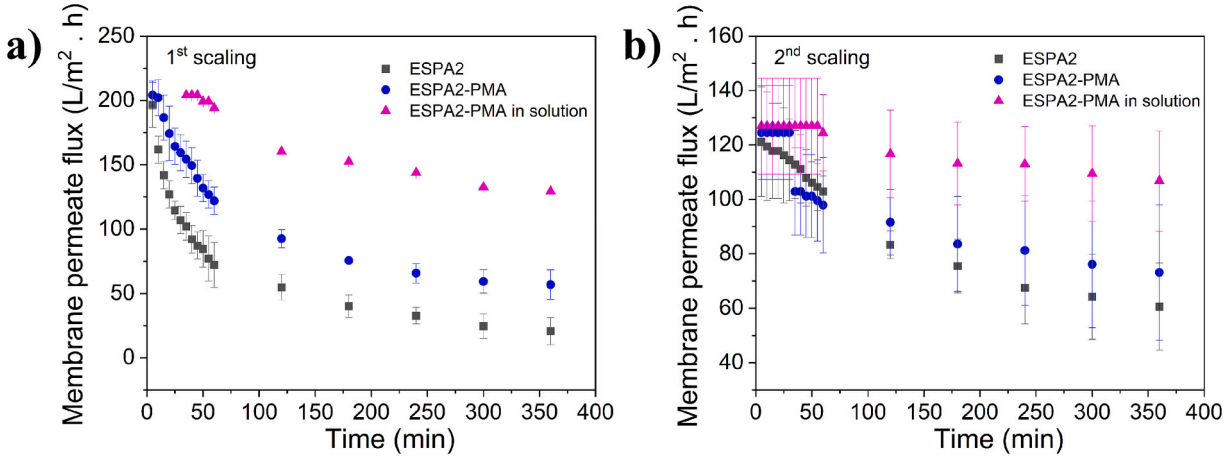

Fig. 3. Membrane performance during gypsum scaling (a) and re-scaling (b) experiments for ESPA2 (bare), ESPA2-PMA (PMA-coated), and ESPA2-PMA_Solution (PMA added to the feed solution). All membranes were tested under identical operating conditions: transmembrane pressure of 500 psi (3.45 MPa), crossflow velocity of 21.4 cm/s, and temperature of 25 °C. The second scaling cycle (b) was performed using the same membrane samples from the first cycle (a), subsequently after an in-situ cleaning step with DIW until a stable permeate flux was reached. In both scaling cycles, the extent of flux decline followed the same trend: ESPA2 > ESPA2-PMA > ESPA2-PMA_Solution, confirming that the addition of PMA to the feed solution provided the greatest resistance to gypsum scaling. Error bars represent standard deviations from triplicate experiments.

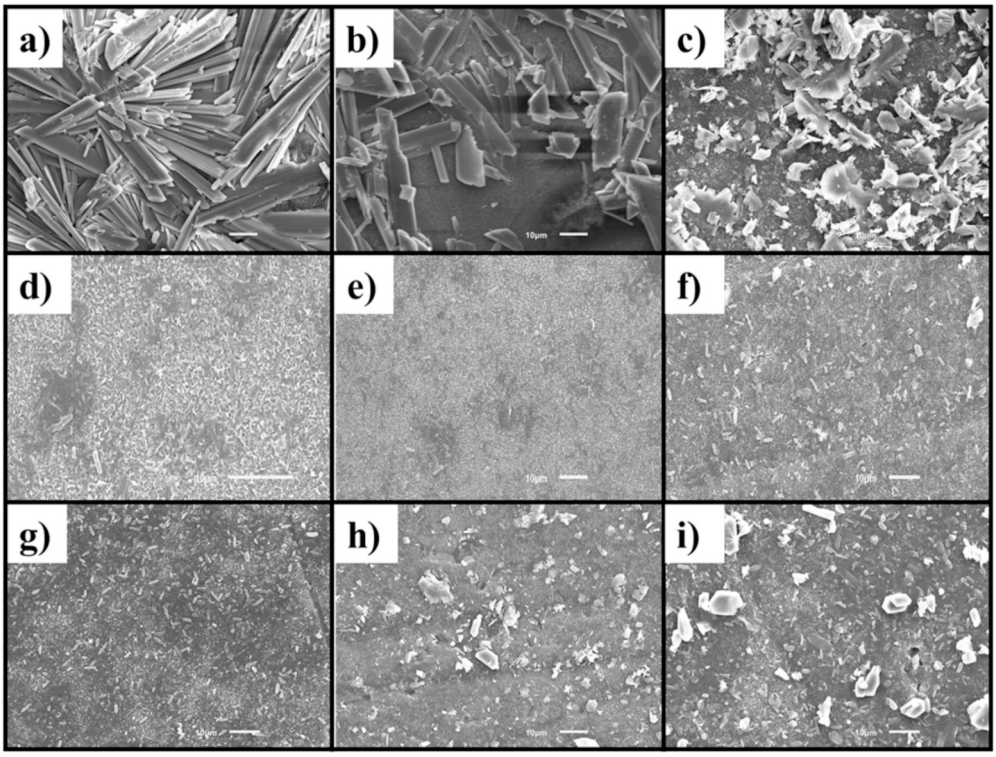

Fig. 4. SEM images of gypsum scaling on membrane surfaces: (a) ESPA2, (b) ESPA2-PMA, and (c) ESPA2-PMA_Solution, after the first gypsum scaling; (d) ESPA2, (e) ESPA2-PMA, and (f) ESPA2-PMA_Solution, after in-situ cleaning; and (g) ESPA2, (h) ESPA2-PMA, and (i) ESPA2-PMA_Solution, after the second gypsum scaling. All images have a scale bar of 10 μm and were taken at 100× magnification.

mineral morphology on all membrane samples after 6 h of gypsum scaling was investigated using SEM. Gypsum crystals formed on bare membrane surfaces (Fig. 4a) exhibited typical well-defined rosette shapes, consisting of plate-like or needle structures that radiate from a central growth point [38,44]. In contrast, irregular plate-like gypsum crystals were observed on PMA-coated membranes, as shown in Fig. 4b [45,46]. These SEM results are consistent with previous findings observed from XRD data. Both measurements coherently demonstrated that PMA coating impacted gypsum crystal morphology formed on membrane surfaces.

Fig. 4c showed that the addition of PMA as an antiscalant resulted in the formation of gypsum crystals on ESPA2-PMA_Solution that were distorted and thicker. These crystals did not resemble the rosette structure observed in the control sample (Fig. 4a). Polymaleic acid appeared to alter the mineral morphology significantly. Other researchers have observed similar modifications in gypsum crystal formations when exposed to carboxylic acids [43,44,46]. For instance, Du et al [47] a reduction in crystal length was observed in the presence of polymaleic acid (PMA). This is because the carboxyl groups of PMA preferentially bind to the (111) face of bassanite, inhibiting its growth along the c-axis. As a result, in the presence of this inhibitor, gypsum growth becomes uneven, with preferential growth along a specific plane due to varying adsorption energies [47,48].

With these differences in gypsum crystal morphology formed on different membranes, the surface coverage by scaling was quantified and linked to the flux decline, as shown in **Fig. S7**. Gypsum precipitate coverage on the ESPA2 membrane surface (73.7 ± 5.3 %) was observed to be higher than on both ESPA2-PMA (65.0 ± 5.7 %) and ESPA2-PMA_Solution (53.1 ± 6.6 %). This observation correlates well with the membrane permeate flux decline presented in Fig. 3a, where the unmodified membrane exhibited a faster flux decline compared to membranes in the presence of PMA (either as a coating agent or an antiscalant additive). The crystals formed on ESPA2-PMA and ESPA2-PMA_Solution are loosely attached to the membrane surface, which allows the water to permeate the membrane surface more readily than in the case of the tight rosette structure present on the bare membrane [11,13].

To reveal the underlying mechanisms for controlling gypsum formation on these membrane surfaces, XPS analysis was performed to investigate the chemical environment of Ca ions across three types of membranes, including ESPA2, ESPA2-PMA, and ESPA2-PMA_Solution after scaling. The high-resolution Ca 2p spectra of the ESPA2 membrane after gypsum scaling, shown in Fig. 5a, revealed characteristic peaks for Ca 2p3/2 at 351.5 eV and Ca 2p1/2 at 347.9 eV. In contrast, for the ESPA2-PMA coated membranes after scaling, these peaks shifted to lower binding energies—347.2 eV for Ca 2p3/2 and 350.8 eV for Ca 2p1/2—indicating that the calcium ions experienced a more electron-rich environment. This shift suggests that the presence of electron-donating groups, such as negatively charged carboxylates ($-COO^-$), increases the local electron density around the calcium ions. For the ESPA2-PMA_Solution membranes, however, both Ca 2p peaks shifted to higher binding energies (348.2 eV for Ca 2p3/2 and 351.9 eV for Ca 2p1/2), reflecting markedly different calcium–PMA interactions depending on whether PMA was surface-grafted or in solution. When PMA is grafted onto the membrane, its fixed carboxyl groups (-COOH) create localized regions of negative charge, providing binding sites for calcium ions and resulting in stable, structured, but spatially limited calcium–carboxylate interactions. In contrast, PMA in solution exhibits greater molecular mobility and conformational flexibility, enabling the formation of dynamic complexes with calcium ions (**Fig. S8**). This increased mobility distributes electron density more broadly within the Ca–PMA complexes, leading to a shift toward higher binding energies [41,49].

These differences in binding energies correlate directly with the observed scaling behavior. The lower binding energies of PMA-coated membranes correspond to restricted, localized calcium interactions, which lead to moderate flux decline. Meanwhile, the higher binding energies for PMA in solution indicate more flexible and distributed

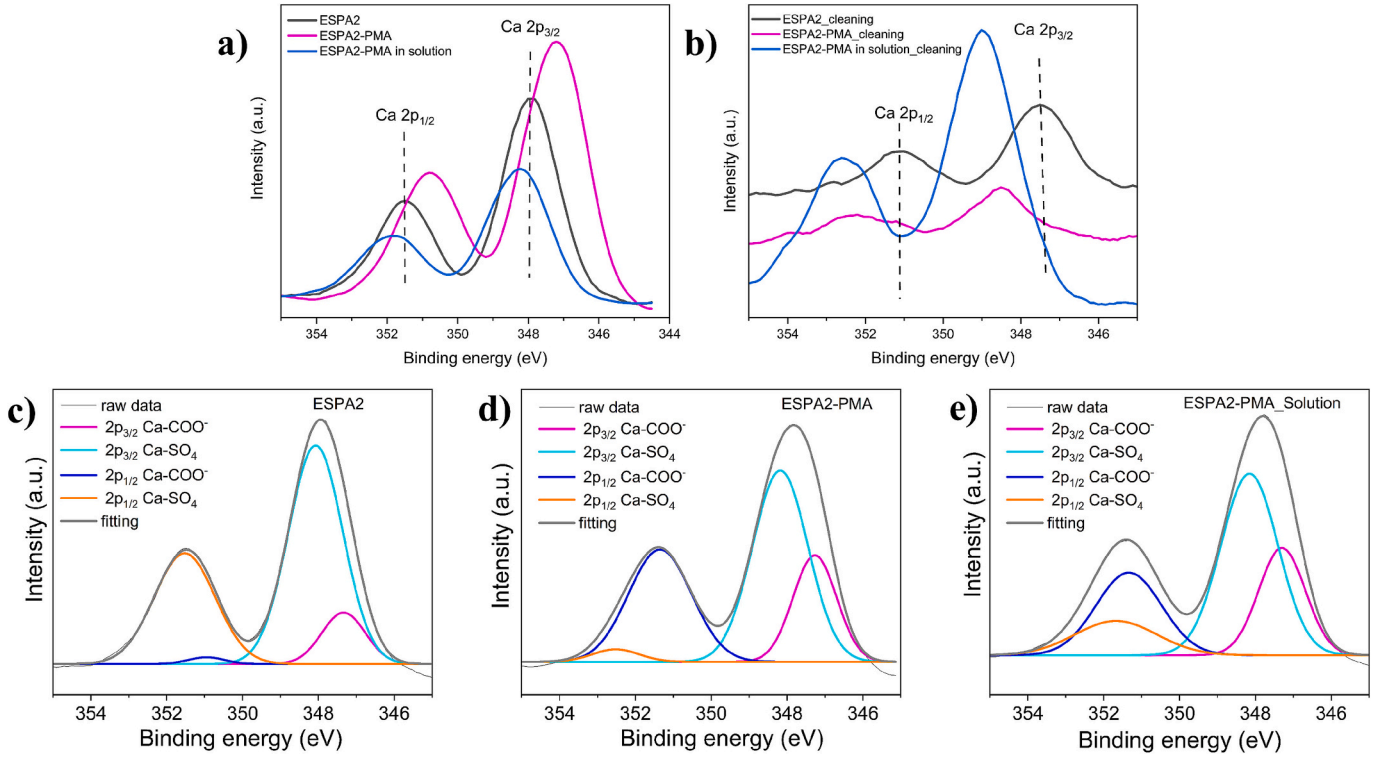

Fig. 5. High-resolution Ca 2p XPS spectra for ESPA2, ESPA2-PMA, and ESPA2-PMA_Solution. Top row: (a) after 6 h of gypsum scaling and (b) after the cleaning process. Bottom row: Ca 2p spectra deconvolution of Ca–SO_4 and Ca–COO^- bindings for (c) ESPA2, (d) ESPA2-PMA, and (e) ESPA2-PMA_Solution.

calcium complexation, effectively inhibiting gypsum growth and resulting in minimal flux decline. These results underscore that both the chemical environment and molecular mobility of PMA critically influence membrane scaling resistance. Similar trends have been reported in the literature: gypsum formation in the presence of carboxylated polymers shifts Ca 2p binding energies to higher values, whereas polycarboxylates immobilized on surfaces tend to shift them lower [38,39]. This behavior can be explained by counterion condensation and conformational constraints. In solution, PMA acts as a flexible polyelectrolyte, attracting counterions such as Ca^{2+}, which increases the energy required to remove electrons and produces a higher binding energy shift. Conversely, when PMA is immobilized on a membrane surface, its reduced conformational flexibility limits counterion condensation, resulting in a lower binding energy shift.

To gain deeper insight into molecular interactions, we analyzed the calcium-binding mechanisms using XPS peak deconvolution of the Ca 2p spectra (Fig. 5c-e). The analysis of the pristine gypsum-scaled membrane revealed two distinct calcium binding environments: Ca-SO_4 and Ca-COO-. The Ca-COO- peak, originating from interactions between calcium and carboxyl groups in the polyamide layer of RO membranes, showed relatively low intensity compared to the Ca-SO_4 peak. In contrast, both PMA-modified scenarios - surface-attached PMA and solution-phase PMA - exhibited higher Ca-COO- binding peaks compared to control, despite the presence of gypsum confirmed by SEM, and XRD (Fig. 4a**, and S6**), which aligns with previous work by Park et al. [50] These results show that both grafted PMA and PMA in solution lead to a clear increase in Ca–COO^- contributions compared to the pristine ESPA2 membrane. While Ca–SO_4 signals remain present, the enhanced Ca–COO^- intensity indicates that PMA promotes stronger calcium–carboxylate interactions at the surface, consistent with the distorted gypsum morphologies observed in SEM (Fig. 4b-c).

3.3. Comparative cleaning efficacy: PMA coated vs. PMA in solution

Following the cleaning process, the normalized permeate recovery percentages for ESPA2, ESPA2-PMA, and ESPA2-PMA_Solution were 82.40 ± 9.8 %, 80.18 ± 11.2 %, and 68.75 ± 1.4 %, respectively (**Fig. S9**). These results indicate that the gypsum precipitates formed on the membranes were removed during the cleaning. Membrane surface characterization techniques, including SEM, FTIR, and XPS, further confirmed this. SEM images showed that, after cleaning, the typical 'ridge-and-valley' pattern of the ESPA2 (Fig. 4d) membrane was retained. In contrast, the ESPA2-PMA membrane (Fig. 4e) exhibited flat surface areas, resulting in smoother membrane characteristics. FTIR analysis also revealed chemical changes on the membrane surfaces post-cleaning (**Fig. S10**). Specifically, a new band at 1700 cm^{-1}, associated with carboxyl (-COOH) groups, appeared on the ESPA2 membrane. These carboxyl groups are intrinsic to the active polyamide layer of commercial membranes and become more exposed after flushing with ultrapure water. Notably, ESPA2-PMA showed a slight increase in the intensity of the -COOH band. This finding was further corroborated by an increase in the O/N ratio (**Table S3**), which rose from 1.6 to 3.2 for ESPA2, implying alterations to the membrane surface, consistent with the FTIR results. In contrast, the O/N ratio for ESPA2-PMA increased only slightly (from 2.4 to 2.8), suggesting that the PMA coating remained stable throughout the scaling and cleaning processes.

The normalized permeate recovery percentages for ESPA2 and ESPA2-PMA did not show a statistically significant difference ($p = 0.401 > 0.05$) (**Fig. S9**). Although ESPA2-PMA exhibited a higher surface –COOH density, its recovery after cleaning was comparable to ESPA2. We hypothesized that the more uniform distribution of –COOH groups in the PMA coating, as indicated by AFM and SEM, which enhanced hydrophilicity and facilitated water sorption. This uniformity and the associated hydration layer likely prevented the formation of tightly anchored deposits, thereby offsetting the stronger Ca^{2+}–COOH interactions typically expected for carboxyl-modified membranes. Although the exact mechanism requires further investigation, the data indicate that the PMA modification does not significantly hinder cleaning under our experimental conditions, consistent with observations in related studies [51,52].The lowest water recovery percentage

observed for ESPA2-PMA_Solution membranes ($p = 0.035 < 0.05$) indicates that water flushing was less effective at removing gypsum crystals from its surface than the unmodified membrane. XPS analysis (Fig. 5b) was performed to investigate the chemical environment of Ca ions across three types of membranes after the in-situ cleaning process to explore the difference in this membrane cleaning performance. The high-resolution Ca 2p3/2 (351.5 eV) and Ca 2p1/2 (347.9) peaks eV for both membranes in the presence of PMA exhibited shifts toward higher binding energy, with the most pronounced shift observed in the PMA-in-solution case. This difference may indicate stronger Ca-PMA interactions, thus leading to the poorer cleaning performance observed for the ESPA2 membranes with PMA added to the solution. Such interactions likely occur through PMA's abundant carboxylate groups, which can (1) calcium ions and (2) bridge gypsum nuclei to the membrane surface (**Fig. S11**), producing deposits more resistant to water flushing.

Furthermore, the N 1 s XPS spectra (**Fig. S12**) provided additional evidence for PMA interaction with the ESPA2 membrane's polyamide layer. The control membrane showed characteristic N 1 s peaks at 399.9 and 401.4 eV. However, after the PMA addition, these peaks shifted to 399.6 and 400.1 eV, respectively. This chemical shift to lower binding energies suggests increased electron density around the nitrogen atoms, consistent with hydrogen bonding between PMA's carboxyl groups (-COOH) and the membrane's amide groups. Additionally, the intensity of the peak around 400 eV was much higher compared to the control, which supports the interaction between PMA and polyamide membrane via non-covalent forces, including hydrogen bonding and electrostatic interactions [53]. Taken together, these observations suggest that PMA in solution not only interacts with gypsum crystals but may also adsorb or form a gel-like layer on the membrane surface, contributing to the hydraulic resistance observed after cleaning. Overall, our study elucidates why PMA in solution presented conflicting behavior: excellent initial scaling prevention followed by poor cleaning efficiency.

3.4. Gypsum re-scaling insights: Membrane durability and crystal morphology

Gypsum re-scaling experiments were conducted to evaluate the membrane reusability after the in-situ cleaning process. The membranes in the subsequent scaling experiment were subjected to the same conditions as the first scaling described previously. The decrease in the non-normalized flux decline (Fig. 3b) for the rescaled membranes followed the same trend as in the first scaling experiment, i.e., ESPA2 < ESPA2-PMA < ESPA2-PMA_Solution. Interestingly, although the flux decline rate presented in the gypsum re-scaling experiment showed the same trend as the first scaling across all membrane samples, the final permeability in the second cycle scaling was higher than their corresponding values related to the first cycle scaling. Notably, for the unmodified membrane, the flux decline decreased from 196.65 ± 17.60 (L/ m^2. h) to 20.66 ± 10.52 (L/ m^2. h) in the first scaling cycle, and from 121.14 ± 20.12 (L/ m^2. h) to 60.60 ± 16.05 (L/ m^2. h) in the subsequent cycle, indicating a substantially less severe performance loss upon re-scaling.

SEM analysis was performed to examine morphological changes in gypsum scaling on the membrane surface after the re-scaling experiment (Fig. 4g-i) to explore the reason behind this phenomenon. Unlike rosette-like and plate-like crystals observed in the first cycle scaling test, only hexagonal short columnar crystals were observed on both the ESPA2-PMA (Fig. 4h) and the ESPA2-PMA_Solution membranes (Fig. 4i). Furthermore, the size of gypsum crystals was notably smaller compared to those formed in the initial cycle of the scaling experiment. The percentage of surface coverage by scaling deposits (**Fig. S7**) also decreased for all samples, with reductions as follows: from 73.3 ± 5.3 % to 42.9 ± 4.8 % for ESPA2, from 65.0 ± 5.7 % to 35.1 ± 1.1 % for ESPA2-PMA, and from 53.1 ± 6.6 % to 24.8 ± 3 % for ESPA2-PMA_Solution. The decline in flux during both the first and second cycles of the gypsum scaling experiment exhibited a linear correlation ($R^2 > 0.95$) (**Fig. S7**) with the surface coverage of mineral precipitates, consistent with the surface blockage model.

These changes in surface scaling coverage can correlate with the reduced flux decline observed during the re-scaling experiments compared to the initial scaling cycle (Fig. 3b). Benecke et al [38] A similar experiment was conducted where the commercial polyamide RO membrane sample was cleaned in situ and subjected to re-scaling experiments. They observed a notable decrease in the diameter of the crystals, simultaneously with an increase in the crystal density, consistent with our observation from SEM images (Fig. 4g-i). Their findings were explained based on two main factors: (1) the in-situ cleaning process physically modified the membrane surface, creating energetically favorable sites for heterogeneous gypsum crystallization and enhancing the membrane's intrinsic nucleation affinity, and (2) the enhanced nucleation affinity also restricted each crystal further growth due to the consumption of scale-forming ions during the early scaling stage. Once the availability of calcium was consumed for nucleation formation, the crystal growth would become restricted. That's why big rosette-like crystals were not found after the rescaling experiments. Therefore, both studies demonstrated how surface modifications caused by the cleaning process and previous scaling events can significantly influence subsequent crystallization kinetics and morphology in membrane re-scaling scenarios.

Our findings regarding the gypsum re-scaling analysis offer significant insights into two key areas. To our knowledge, this was the first time a modified commercial polyamide membrane had been subjected to a re-scaling experiment. Secondly, our results reveal a notable performance advantage. Despite all membranes experiencing surface physical and chemical alterations due to the cleaning process, the PMA-coated membrane exhibited a superior flux decline rate compared to the bare membrane. This indicates not only the effectiveness of the PMA coating but also its stability under re-scaling conditions, highlighting its potential for enhanced membrane durability and performance in practical applications.

4. Conclusion

This study examined the role of PMA in mitigating gypsum scaling in RO membranes using two approaches: as a surface coating (ESPA2-PMA) and as an antiscalant in solution (ESPA2-PMA_Solution). The work is novel in evaluating PMA in both immobilized and soluble forms, as well as assessing membrane performance after cleaning and re-scaling to reveal the long-term stability and effectiveness of PMA modification. Our findings demonstrate that both PMA applications effectively reduced gypsum scaling, with PMA in solution exhibiting the highest scaling resistance (maintaining up to 70 % of the initial flux after 6 h), followed by the PMA-coated membrane (26.6 %) and the unmodified control (15.2 %). However, the cleaning experiments revealed critical differences in membrane performance and stability. While PMA in solution provided superior scaling resistance, it resulted in a lower cleaning efficiency, with only 68.7 % water flux recovery compared to 82.4 % for the unmodified membrane. This was attributed to the potential interaction between PMA (as antiscalant agent) and membrane, which hindered complete gypsum removal during cleaning.

In contrast, the PMA coating demonstrated stability through cleaning cycle, as confirmed by FTIR. After cleaning, the unmodified ESPA2 membrane exhibited a new band at 1700 cm^{-1}, associated with carboxyl (-COOH) groups, indicating exposure of the intrinsic polyamide layer. By comparison, ESPA2-PMA showed a slight increase in the -COOH band intensity, suggesting that the coating remained intact. In re-scaling experiments, the PMA-coated membrane also displayed enhanced resistance to gypsum deposition relative to the control, highlighting its potential for long-term use. SEM analysis further revealed that gypsum crystals formed after re-scaling were smaller and exhibited altered morphologies, indicating that prior scaling–cleaning cycles influence

subsequent mineralization. Together, these results provide insights into the long-term effects of PMA on RO membrane performance, emphasizing the interplay between scaling prevention, cleaning efficiency, and coating stability. The results highlight the potential of PMA coatings as a durable strategy for improving membrane longevity, pointing to the need for optimized cleaning protocols when using PMA as a feed additive. Future studies should further investigate the mechanisms governing gypsum re-scaling behavior and explore alternative cleaning strategies to maximize scaling resistance and fouling reversibility.

CRediT authorship contribution statement

Raynara Maria Silva Jacovone: Writing – original draft, Visualization, Investigation, Formal analysis. **Meng Wang:** Writing – review & editing, Visualization, Investigation. **Jaqueline Jamara Souza Soares:** Formal analysis. **Solange Kazumi Sakata:** Writing – review & editing, Validation, Supervision, Methodology, Funding acquisition, Conceptualization. **Debora Frigi Rodrigues:** Writing – review & editing, Validation, Supervision, Methodology, Funding acquisition, Conceptualization.

Funding

This study was funded by Qatar National Research Fund (NPRP12S-0307-190250), the National Science Foundation under Grant No. CHE-1904472, and National Council for the Improvement of Higher Education – CAPES (Finance Code 001).

Declaration of competing interest

The authors declare that they have no known competing financial interests or personal relationships that could have appeared to influence the work reported in this paper.

Acknowledgments

The authors thank Dr. Richard Franks from Hydranautics Inc. for providing the membrane for this research study. We also thank Dr. Yan Yao and Dr. Jacinta Conrad and their students for granting us access to the XRD equipment and the contact angle goniometer, respectively. Moreover, the authors would like to thank BioRender.com for providing the tools used to create the abstract graphic and illustrations shown in the Supporting Information.

Appendix A. Supplementary data

Experimental details, including PMA coating synthesis and optimization, TBO measurement detailed protocol and results. Supplementary data to this article can be found online at https://doi.org/10.1016/j.desal.2025.119544.

Data availability

Data will be made available on request.

References

[1] M. Asadollahi, D. Bastani, S.A. Musavi, Enhancement of surface properties and performance of reverse osmosis membranes after surface modification: a review, Desalination 420 (2017) 330–383, https://doi.org/10.1016/j.desal.2017.05.027.
[2] W. Yu, W. Chen, H. Yang, Evaluation of structural effects on the antiscaling performance of various graft cellulose-based antiscalants in RO membrane scaling control, J. Memb. Sci. 620 (2021) 118893, https://doi.org/10.1016/j.memsci.2020.118893.
[3] M. Tawalbeh, L. Qalyoubi, A. Al-Othman, M. Qasim, M. Shirazi, Insights on the development of enhanced antifouling reverse osmosis membranes: industrial applications and challenges, Desalination 553 (2023) 116460, https://doi.org/10.1016/j.desal.2023.116460.
[4] M. Wang, B. Cao, Y. Hu, D.F. Rodrigues, Mineral scaling on reverse osmosis membranes: role of mass, orientation, and crystallinity on permeability, Environ. Sci. Technol. 55 (2021) 16110–16119, https://doi.org/10.1021/acs.est.1c04143.
[5] V. Karanikola, C. Boo, J. Rolf, M. Elimelech, Engineered slippery surface to mitigate gypsum scaling in membrane distillation for treatment of hypersaline industrial wastewaters, Environ. Sci. Technol. 52 (2018) 14362–14370, https://doi.org/10.1021/acs.est.8b04836.
[6] T. Tong, A.F. Wallace, S. Zhao, Z. Wang, Mineral scaling in membrane desalination: mechanisms, mitigation strategies, and feasibility of scaling-resistant membranes, J. Memb. Sci. 579 (2019) 52–69, https://doi.org/10.1016/j.memsci.2019.02.049.
[7] S. Jiang, Y. Li, B.P. Ladewig, A review of reverse osmosis membrane fouling and control strategies, Sci. Total Environ. 595 (2017) 567–583, https://doi.org/10.1016/j.scitotenv.2017.03.235.
[8] S.A. Kaushik, D. Armbruster, J. Dittmer, D. Bruniecka-Sulewski, B. Wendler, M. Ernst, Investigation of scaling inhibition and biofouling potential of different molecular weight fractions of a PAA antiscalant, NPJ Clean Water. 7 (2024) 36, https://doi.org/10.1038/s41545-024-00332-7.
[9] Z. Amjad, P.G. Koutsoukos, Evaluation of maleic acid based polymers as scale inhibitors and dispersants for industrial water applications, Desalination 335 (2014) 55–63, https://doi.org/10.1016/j.desal.2013.12.012.
[10] T. Rabizadeh, C.L. Peacock, L.G. Benning, Carboxylic acids: effective inhibitors for calcium sulfate precipitation? Mineral. Mag. 78 (2014) 1465–1472, https://doi.org/10.1180/minmag.2014.078.6.13.
[11] Y. Yin, S. Kalam, J.L. Livingston, R. Minjarez, J. Lee, S. Lin, T. Tong, The use of anti-sealants in gypsum scaling mitigation: comparison with membrane surface modification and efficiency in combined reverse osmosis and membrane distillation, J. Memb. Sci. 643 (2022) 120077, https://doi.org/10.1016/j.memsci.2021.120077.
[12] W. Yu, D. Song, W. Chen, H. Yang, Antiscalants in RO membrane scaling control, Water Res. 183 (2020) 115985, https://doi.org/10.1016/j.watres.2020.115985.
[13] D.L. Shaffer, M.E. Tousley, M. Elimelech, Influence of polyamide membrane surface chemistry on gypsum scaling behavior, J. Memb. Sci. 525 (2017) 249–256, https://doi.org/10.1016/j.memsci.2016.11.003.
[14] A. Ansari, J. Peña Bahamonde, M. Wang, D.L. Shaffer, H. Yandi, D.F. Rodrigues, Polyacrylic acid-brushes tethered to graphene oxide membrane coating for scaling and biofouling mitigation on reverse osmosis membranes, J. Memb. Sci. 630 (2021) 119308, https://doi.org/10.1016/j.memsci.2021.119308.
[15] A. Benbakhti, T. Bachir-Bey, Synthesis and characterization of maleic acid polymer for use as scale deposits inhibitors, J. Appl. Polym. Sci. 116 (2010) 2658–2667, https://doi.org/10.1002/app.
[16] M.Y. Ashfaq, M.A. Al-Ghouti, Effect of polymaleic acid and microwave radiations on reverse osmosis membrane's performance and properties: a response surface methodology approach, Desalination 550 (2023) 116372, https://doi.org/10.1016/j.desal.2023.116372.
[17] M.Y. Ashfaq, M.A. Al-Ghouti, N. Zouari, Investigating the effect of polymer-modified graphene oxide coating on RO membrane fouling, J Water Process Eng 49 (2022) 103164, https://doi.org/10.1016/j.jwpe.2022.103164.
[18] D. Chen, C.Q. Yang, X. Qiu, Aqueous polymerization of maleic acid and cross-linking of cotton cellulose by poly(maleic acid), Ind. Eng. Chem. Res. 44 (2005) 7921–7927, https://doi.org/10.1021/ie050651+.
[19] T. Tong, S. Zhao, C. Boo, S.M. Hashmi, M. Elimelech, Relating silica scaling in reverse osmosis to membrane surface properties, Environ. Sci. Technol. 51 (2017) 4396–4406, https://doi.org/10.1021/acs.est.6b06411.
[20] A. Fakhru'L-Razi, I.Y.M. Qudsieh, W.M.Z.W. Yunus, M.B. Ahmad, M.Z.A. Rahman, Graft copolymerization of methyl methacrylate onto sago starch using ceric ammonium nitrate and potassium persulfate as redox initiator systems, J. Appl. Polym. Sci. 82 (2001) 1375–1381, https://doi.org/10.1002/app.1974.
[21] R. Vasallo-Antonio, J. Peña-Bahamonde, M.D. Susman, F.C. Ballesteros, D. F. Rodrigues, Design and performance of Fe3O4@SiO2/MoO3/polydopamine-graphene oxide composites for visible light photocatalysis, Emerg. Mater. 4 (2021) 1425–1439, https://doi.org/10.1007/s42247-020-00142-w.
[22] M.Y. Ashfaq, M.A. Al-Ghouti, Optimization of Polyacrylic acid coating on graphene oxide-functionalized reverse-osmosis membrane using UV radiation through response surface methodology, Polymers 14 (2022) 3711, https://doi.org/10.3390/polym14183711.
[23] H. Oesinghaus, E.E. Eiden, T. Kratky, M.J. Huber, S. Schrettl, S. Holz, M. Elsner, K. Glas, Analytical characterization of damage in reverse osmosis membranes caused by components of a chlorine dioxide matrix, Desalin. Water Treat. 320 (2024) 100633, https://doi.org/10.1016/j.dwt.2024.100633.
[24] C. Dai, A.G. Stack, A. Koishi, A. Fernandez-Martinez, S.S. Lee, Y. Hu, Heterogeneous nucleation and growth of barium sulfate at organic-water interfaces: interplay between surface hydrophobicity and Ba2+ adsorption, Langmuir 32 (2016) 5277–5284, https://doi.org/10.1021/acs.langmuir.6b01036.
[25] M. Wang, X. Zuo, R.M.S. Jacovone, R. O'Hara, A.N. Mondal, A. Asatekin, D. F. Rodrigues, Influence of zwitterionic amphiphilic copolymers on heterogeneous gypsum formation: a promising approach for scaling resistance, Water Res. 266 (2024) 122439, https://doi.org/10.1016/j.watres.2024.122439.
[26] M. Wang, H. Nguyen, S.J. Lounder, A. Asatekin, D.F. Rodrigues, Calcium sulfate formation on different Zwitterionic amphiphilic copolymer substrates for salt water treatment, ACS Appl. Polym. Mater. 4 (2022) 7090–7101, https://doi.org/10.1021/acsapm.2c01014.
[27] B. Cao, A. Ansari, X. Yi, D.F. Rodrigues, Y. Hu, Gypsum scale formation on graphene oxide modified reverse osmosis membrane, J. Memb. Sci. 552 (2018) 132–143, https://doi.org/10.1016/j.memsci.2018.02.005.
[28] T. Rabizadeh, D.J. Morgan, C.L. Peacock, L.G. Benning, Effectiveness of green additives vs poly(acrylic acid) in inhibiting calcium sulfate Dihydrate

crystallization, Ind. Eng. Chem. Res. 58 (2019) 1561–1569, https://doi.org/10.1021/acs.iecr.8b02904.
[29] Y. Ji, X. Yang, Z. Ji, L. Zhu, N. Ma, D. Chen, X. Jia, J. Tang, Y. Cao, DFT-calculated IR spectrum amide I, II, and III band contributions of N-methylacetamide fine components, ACS Omega. 5 (2020) 8572–8578, https://doi.org/10.1021/acsomega.9b04421.
[30] A. Matin, H.Z. Shafi, Z. Khan, M. Khaled, R. Yang, K. Gleason, F. Rehman, Surface modification of seawater desalination reverse osmosis membranes: characterization studies & performance evaluation, Desalination 343 (2014) 128–139, https://doi.org/10.1016/j.desal.2013.10.023.
[31] A. Antony, R. Fudianto, S. Cox, G. Leslie, Assessing the oxidative degradation of polyamide reverse osmosis membrane-accelerated ageing with hypochlorite exposure, J. Memb. Sci. 347 (2010) 159–164, https://doi.org/10.1016/j.memsci.2009.10.018.
[32] H. Majid, N. Heidarzadeh, V. Vatanpour, A. Dehqan, Surface modification of commercial reverse osmosis membranes using both hydrophilic polymer and graphene oxide to improve desalination efficiency, Chemosphere 302 (2022) 134931, https://doi.org/10.1016/j.chemosphere.2022.134931.
[33] M. Tian, H.J. Xu, L. Yao, R. Wang, A biomimetic antimicrobial surface for membrane fouling control in reverse osmosis for seawater desalination, Desalination 503 (2021) 114954, https://doi.org/10.1016/j.desal.2021.114954.
[34] X. Li, Y. Chen, J. Zou, X. Zeng, L. Zhou, H. Huang, Stable freestanding Li-ion battery cathodes by in situ conformal coating of conducting polypyrrole on NiS-carbon nanofiber films, J. Power Sources 331 (2016) 360–365, https://doi.org/10.1016/j.jpowsour.2016.09.067.
[35] Y. Sun, W. Song, F. Gao, X. Wang, X. Luo, J. Guo, B. Zhang, J. Shi, C. Cheng, Q. Liu, S. Li, In situ conformal coating of polyaniline on GaN microwires for ultrafast, self-driven heterojunction ultraviolet photodetectors, ACS Appl. Mater. Interfaces 12 (2020) 13473–13480, https://doi.org/10.1021/acsami.9b21796.
[36] H. Jaramillo, C. Boo, S.M. Hashmi, M. Elimelech, Zwitterionic coating on thin-film composite membranes to delay gypsum scaling in reverse osmosis, J. Memb. Sci. 618 (2021) 118568, https://doi.org/10.1016/j.memsci.2020.118568.
[37] Y. Yin, T. Li, K. Zuo, X. Liu, S. Lin, Y. Yao, T. Tong, Which surface is more scaling resistant? A closer look at nucleation theories for heterogeneous gypsum nucleation in aqueous solutions, Environ. Sci. Technol. 56 (2022) 16315–16324, https://doi.org/10.1021/acs.est.2c06560.
[38] J. Benecke, M. Haas, F. Baur, M. Ernst, Investigating the development and reproducibility of heterogeneous gypsum scaling on reverse osmosis membranes using real-time membrane surface imaging, Desalination 428 (2018) 161–171, https://doi.org/10.1016/j.desal.2017.11.025.
[39] V.I. Kalikmanov, in: V.I. Kalikmanov (Ed.), Classical Nucleation Theory BT - Nucleation Theory, Springer Netherlands, 2013, pp. 17–41, https://doi.org/10.1007/978-90-481-3643-8_3. Dordrecht.
[40] Y. Hu, C. Neil, B. Lee, Y.S. Jun, Control of heterogeneous Fe(III) (hydr)oxide nucleation and growth by interfacial energies and local saturations, Environ. Sci. Technol. 47 (2013) 9198–9206, https://doi.org/10.1021/es401160g.
[41] B. Zhao, W.J. Brittain, Polymer brushes: surface-immobilized macromolecules, Prog. Polym. Sci. 25 (2000) 677–710, https://doi.org/10.1016/S0079-6700(00)00012-5.
[42] J.C. Conrad, M.L. Robertson, Shaping the structure and response of surface-grafted polymer brushes via the molecular weight Distribution, JACS Au (2023) 333–343, https://doi.org/10.1021/jacsau.2c00638.
[43] M. Inoue, I. Hirasawa, The relationship between crystal morphology and XRD peak intensity on CaSO4·2H2O, J. Cryst. Growth 380 (2013) 169–175, https://doi.org/10.1016/j.jcrysgro.2013.06.017.
[44] W.Y. Shih, A. Rahardianto, R.W. Lee, Y. Cohen, Morphometric characterization of calcium sulfate dihydrate (gypsum) scale on reverse osmosis membranes, J. Memb. Sci. 252 (2005) 253–263, https://doi.org/10.1016/j.memsci.2004.12.023.
[45] A. Saha, J. Lee, S.M. Pancera, M.F. Bräeu, A. Kempter, A. Tripathi, A. Bose, New insights into the transformation of calcium sulfate hemihydrate to gypsum using time-resolved cryogenic transmission electron microscopy, Langmuir 28 (2012) 11182–11187, https://doi.org/10.1021/la3024474.
[46] Y.W. Wang, F.C. Meldrum, Additives stabilize calcium sulfate hemihydrate (bassanite) in solution, J. Mater. Chem. 22 (2012) 22055–22062, https://doi.org/10.1039/c2jm34087a.
[47] J. Du, L. Tian, M. Qi, C. Zhang, H. Di, X. Zhi, J. Zhu, Revealing maleic acid role in the preparation of α-hemihydrate gypsum from titanium gypsum through experiments and DFT calculations, Sci. Total Environ. 897 (2023) 166405, https://doi.org/10.1016/j.scitotenv.2023.166405.
[48] X. Li, W. Gao, Conversion of phosphogypsum into α-hemihydrate in the presence of potassium acid phthalate and Ca2+: experimental and DFT studies, Colloids Surfaces A Physicochem. Eng. Asp. 652 (2022) 129906, https://doi.org/10.1016/j.colsurfa.2022.129906.
[49] M.P.C. Weijnen, G.M. van Rosmalen, The influence of various polyelectrolytes on the precipitation of gypsum, Desalination 54 (1985) 239–261, https://doi.org/10.1016/0011-9164(85)80021-7.
[50] S. Park, M. Saavedra, X. Liu, T. Li, B. Anger, T. Tong, A comprehensive study on combined organic fouling and gypsum scaling in reverse osmosis: decoupling surface and bulk phenomena, J. Memb. Sci. 694 (2024) 122399, https://doi.org/10.1016/j.memsci.2023.122399.
[51] Y.H. Chiao, M. Hu, R.R. Gonzales, Z. Yang, H. Matsuyama, Gypsum scaling behavior of the tannic acid-coated polyamide reverse osmosis membrane, ACS ES T Water. 4 (2024) 237–244, https://doi.org/10.1021/acsestwater.3c00568.
[52] Y. Chen, Y. Cohen, Calcium sulfate and calcium carbonate scaling of thin-film composite polyamide reverse osmosis membranes with surface-tethered Polyacrylic acid chains, Membranes 12 (2022) 1287, https://doi.org/10.3390/membranes12121287.
[53] S.M. Gericke, W.D. Mulhearn, D.E. Goodacre, J. Raso, D.J. Miller, L. Carver, S. Nemšák, O. Karslioğlu, L. Trotochaud, H. Bluhm, C.M. Stafford, C. Buechner, Water-polyamide chemical interplay in desalination membranes explored by ambient pressure X-ray photoelectron spectroscopy, Phys. Chem. Chem. Phys. 22 (2020) 15658–15663, https://doi.org/10.1039/d0cp01842b.